Materials Science & Engineering A 626 (2015) 150–158

Contents lists available at ScienceDirect

Materials Science & Engineering A

journal homepage: www.elsevier.com/locate/msea

Nanomechanical behavior of 3D porous metal–ceramic nanocomposite Bi/Bi_2O_3 films

R. Domingo-Roca [a], D. Esqué-de los Ojos [a,*], M. Guerrero [a,*], E. Pellicer [a], M.D. Baró [a], S. Suriñach [a], J. Sort [b]

[a] Departament de Física, Universitat Autònoma de Barcelona, E-08193 Bellaterra, Spain
[b] Institució Catalana de Recerca i Estudis Avançats (ICREA) and Departament de Física, Universitat Autònoma de Barcelona, E-08193 Bellaterra, Spain

ARTICLE INFO

Article history:
Received 16 October 2014
Received in revised form
9 December 2014
Accepted 13 December 2014
Available online 23 December 2014

Keywords:
Metal/metal oxide composite
Nanoindentation
Loading rate
Mechanical properties
Viscoelastic non-Newtonian behavior
Finite element simulations

ABSTRACT

The nanomechanical properties of three-dimensional (3D) porous metal/metal oxide composite (Bi/Bi_2O_3) films grown by direct current electrodeposition have been studied by nanoindentation at two different loading rates. The synthesized films exhibit a mixture of crystallographic phases of metallic Bi and α-Bi_2O_3, as evidenced by X-ray diffraction. An in-situ compaction of the sample during the nanoindentation assays has been observed. This in-situ compaction has an influence over both the hardness and elastic modulus of the material, being more important on the latter and, therefore, on the determination of the degree of porosity of the composite film. The influence of the loading rate on the mechanical properties has been investigated. In addition, time-dependent deformation processes (creep tests) have been also performed, revealing an anelastic behavior irrespective of the loading rate. From these creep tests, a viscoelastic non-Newtonian behavior of the sample is evidenced, which is well-described by a three-element Voigt model.

1. Introduction

Three-dimensional (3D) porous films have become increasingly popular in the last years as they offer a large number of applications in electrocatalysis [1], separation and concentration of gas molecules [2], batteries [3], sensors [4], electronic devices [5] and even in magnetic applications in which the surface area plays an important role [6]. Several strategies are currently being pursued for the preparation of porous films like de-alloying [7], galvanic replacement [8] or templating [9].

The vast majority of the studied porous materials are: (i) polymers (used for example for bone tissue engineering [10]); (ii) metallic foams, which can be produced through several routes such as de-alloying, electrodeposition or vapor deposition [11], presenting different structures (as wires or spheres) [12] and they are used as high temperature resistant materials or biomaterials, among others; and (iii) metal oxides, which can be synthesized in several ways [13] such as soft templating [14], anodic oxidation of Al and Ti to obtain porous anodic alumina membranes (PAA) [15–18] or TiO_2 nanotubes [19–21] and reinforced crystallization method [22] using a silica/carbon enforcement method [12,23]. In the last years, metal oxide materials have become increasingly studied as they present a wide range of applications, namely in solar cells [24–26], supercapacitors [27] or catalytic processes [28,29]. Many of these applications can be improved by providing porosity to the material. Besides the degree of porosity and pore size, the orientation and distribution of pores also have an important influence on the mechanical properties of the composites and, consequently, on their applications. Interestingly, porous multi-phase or composite materials, particularly porous metal–ceramic materials, have not been thoroughly studied yet. These composites are important due the synergy of properties between the components of the material and the surface/interphase interactions. In the metal–ceramic composite materials, mechanical properties are convoluted, presenting a relatively high hardness (ceramic phase) and ductility (metal phase).

Irrespectively of the application, the mechanical properties of porous materials are of paramount importance for the robustness and integrity of any device. Despite the porous coatings have been used as impact dampers [30,31], porous materials of finite dimensions are usually brittle. Because of this fragility, the study of the mechanical properties of porous materials is very challenging: they usually break under tension or torsion. An additional problem stems from the modification of the degree of porosity of the material when it is loaded in compression, thus making it difficult to assess the intrinsic mechanical properties of the pristine material. For all these reasons, the most appropriate method to

* Corresponding authors.
E-mail addresses: Daniel.Esque@uab.cat (D. Esqué-de los Ojos), Miguel.Guerrero@uab.cat (M. Guerrero).

http://dx.doi.org/10.1016/j.msea.2014.12.042
0921-5093/

measure the mechanical properties of porous materials is nanoindentation [15,32–39]. Nanoindentation has been widely used to measure the mechanical properties of coatings because of its many advantages over conventional methods [40]. Namely it can deform materials on a very small scale. The assessment of the mechanical properties of porous materials using nanoindentation is a challenge since a densified zone is formed underneath the indenter during indentation. Nevertheless, a good correlation between hardness and elastic modulus with both the degree of porosity and pore geometry has been established. Fleck et al. [41] studied the effect of porosity on indentation and they found that the average indentation pressure increases as the level of initial porosity decreases when the indentation is performed on bulk materials with known elastic modulus and porosity.

Previous works have reported on the mechanical characterization of porous metal oxide films and it has been shown that both hardness (H) and reduced elastic modulus (E_r) decrease monotonically as the mean pore diameter increases [15]. Some works have pointed out that the densification has some important implications on H but not so much on E_r [42]. Meanwhile other authors have reported the opposite trend [43]. These studies suggest that special care should be taken when assessing the effect of porosity on indentation of porous materials and further investigation of these issues is required. The mechanical properties of this kind of materials typically depend both on the pore shape and size, as well as on the interconnections between solid regions. Furthermore, the influence of the test's loading rate on the mechanical properties of porous materials has not been systematically studied. Almost all the previous studies on the effects of indentation strain rate have been performed on metallic foams [44], and not on metal–ceramic composites.

In this paper, porous metal/metal oxide Bi/Bi_2O_3 composite films, with a thickness of 130 μm, have been synthesized by means of electrodeposition. Both the structural and morphological properties of the Bi/Bi_2O_3 composite film have been characterized by X-ray diffraction (XRD) and scanning electron microscopy (SEM) techniques, respectively. Also the mechanical properties have been determined using nanoindentation tests at two different loading rates. The method of Oliver and Pharr [45] has been applied to determine the mechanical properties (both H and E_r). The values of the elastic modulus have been used to estimate the degree of porosity of the sample, as well as its variation as a function of the applied load. In addition, time-dependent deformation processes during nanoindentation have been investigated in order to study the anelastic behavior (elasticity that depends on time) of the sample and a behavior analogous to a viscoelastic non-Newtonian fluid has been observed. Finally, finite element (FE) simulations of Berkovich indentation have been used to study the variation of the mechanical properties as a function of the applied load and, consequently, as a function of the penetration depth.

2. Materials and methods

2.1. Preparation of Bi/Bi_2O_3

Bi/Bi_2O_3 composite was obtained by direct current electrodeposition in a thermostatized one-compartment three-electrode cell using a PGSTAT302N Autolab potentiostat/galvanostat (Ecochemie). The working electrode was positioned vertically within the electrolyte and consisted of 5 mm × 6 mm Si chips (crystal orientation 100), on top of which a Ti adhesion layer of 50 nm and a Au seed-layer of 500 nm had been successively deposited through e-beam evaporation. The working area was 0.25 cm^2. A double junction Ag|AgCl ($E = +0.210$ V/SHE) reference electrode (Metrohm AG) was used with 3 M potassium chloride (KCl) inner solution and an interchangeable outer solution. The outer solution was made of 1 M sodium chloride (NaCl). A platinum sheet served as counter electrode. The electrolyte contained 1.2 M HCl, $8 \cdot 10^{-3}$ M $BiCl_3$, $2 \cdot 10^{-2}$ M NaCl and variable amounts of Triton X-100. Triton X-100 ($C_{14}H_{22}O(C_2H_4O)_n$) is a nonionic surfactant that has a hydrophilic polyethylene oxide chain and an aromatic hydrocarbon hydrophobic group. The sample was obtained galvanostatically by applying a constant current density of $-1\ A \cdot cm^{-2}$. Deposition was conducted at room temperature under vigorous stirring (5000 rpm) using a magnetic stirrer bar. Prior to deposition, the Au surface was degreased with acetone and dried with a soft tissue. The Si backside was insulated by painting it with a nonconductive ink to ensure only the Au surface was conductive.

2.2. Morphological and structural characterization

The morphology of the deposits was studied by SEM using a Zeiss Merlin microscope. The structure and phase percentages of the powders were assessed by XRD using an X'Pert Philips diffractometer and Cu K_α radiation, in the Bragg–Brentano geometry operating in the step scan mode. The phase percentages of the composite film were quantified from the XRD patterns by means of a data analysis program based on a full pattern fitting procedure (Rietveld method) using the MAUD software [46]. The chemical composition of the film was determined by Energy Dispersive X-Ray Spectroscopy (EDX).

2.3. Mechanical characterization

Mechanical properties of the Bi/Bi_2O_3 films were evaluated using a nanoindenter (UMIS) from Fischer–Cripps Laboratory and the obtained data was treated with the IBIS software.

Force displacement load-unload curves were measured for different conditions in load control mode using a calibrated Berkovich tip made of single crystalline diamond. The values of H and E_r were evaluated, using the method of Oliver and Pharr [45]. The obtained data was treated in order to correct for the thermal drift (which was lower than 0.05 nm/s during nanoindentation), the instrument compliance, the indenter shape function (i.e., blunting of the tip) and the initial penetration depth (a pre-contact of 0.2 mN was applied to detect the surface). Two different conditions (slow and fast) were used reaching maximum loads (P_{max}) between 1 mN and 5 mN in steps of 0.2 mN, allowing the study of the variation of H and E_r as a function of P_{max}. The tests were programmed using different loading rates, indenting the sample in arrays of 17 × 17 indents which were separated from each other by 70 μm. This separation between indents was imposed in order to avoid the influence of neighboring indentations. On the other hand, the creep tests (performed to study the anelastic behavior of the sample) consisted in indenting the sample at a constant load of 5 mN, in arrays of 5 × 5 indents which were separated from each other by 120 μm, also at different loading rates.

H and E_r were derived from the method of Oliver and Pharr, using the unloading stage of the load–displacement curves, in which it is assumed that only elastic deformation is occurring on the material. From the initial unloading slope, the contact stiffness (S) was determined as:

$$S = \frac{dP}{dh} \tag{1}$$

where P and h are the applied force and the penetration depth during the nanoindentation test, respectively. The reduced elastic modulus has a relation with the projected contact area A and the

contact stiffness, so it can be evaluated as:

$$S = \beta \frac{2}{\sqrt{\pi}} E_r \sqrt{A} \tag{2}$$

where β is the so-called King's factor, which depends on the indenter's geometry and has a value of 1.034 for the Berkovich tip [47]. Also the reduced elastic modulus takes into account the elastic displacement that occurs in both sample and indenter:

$$\frac{1}{E_r} = \frac{1-\nu_m^2}{E_m} + \frac{1-\nu_i^2}{E_i} \tag{3}$$

where subindexes m and i refer to the material and indenter, respectively, and ν is the Poisson's ratio. The hardness was determined using the following expression:

$$H = \frac{P_{max}}{A} \tag{4}$$

where P_{max} is the maximum applied force during nanoindentation and A is the projected contact area between the indenter and the material.

2.4. Finite element simulations

While indenting a porous material, it is reasonable to assume that its mechanical properties will change as a result of compaction. In order to study this variation, we performed Berkovich indentation finite element simulations with the commercial ABAQUS© software [48]. As the response of the material was supposed to be isotropic under indentation, we considered an axisymmetric model consisting of 37,060 linear four-node fully-integrated elements (CAX4). A mesh-refinement technique was used to ensure both, optimal resolution during contact and reasonable computational time. The indenter was modeled as a rigid cone with a characteristic angle equal to 70.32° to reproduce the response of a Berkovich indenter in a three-dimensional model. Contact between indenter and material was chosen to be frictionless and the load is applied by displacing the indenter. Two models were selected while studying the experimental P–h_s curves: (i) an elastic–perfectly plastic model (Eq. (5)), being the input mechanical properties Young's modulus (E) and the yield stress (σ_{ys}) of the material, and (ii) incorporating an associated linear Drucker–Prager (DP) criterion (Eq. (6)), where E, the frictional angle (β) and σ_{ys} are the required mechanical properties. Basically, what the DP criterion provides is a pressure-sensitive model in which the yield surface changes with the hydrostatic pressure according to a frictional angle. In other words, as the material compacts (increase of hydrostatic pressure) the yield surface changes. DP is extensively used during modelling of porous materials [49–51].

$$\varepsilon = \begin{cases} \sigma/E & \text{if } \sigma < \sigma_{ys} \\ \sigma/\sigma_{ys} & \text{if } \sigma > \sigma_{ys} \end{cases} \tag{5}$$

$$F = \frac{1}{2}\sqrt{\frac{3}{2}(\boldsymbol{S}:\boldsymbol{S})} - p\ \tan\beta - d \tag{6}$$

Being F the yield surface, $\boldsymbol{S}$ the deviatoric stress tensor, p the hydrostatic pressure and d the cohesion expressed as

$$d = \left(1 - \tfrac{1}{3}\ \tan\beta\right)\sigma_{ys} \tag{7}$$

Regardless of the used model, the values for E and σ_{ys} were considered to change with the applied load.

3. Results and discussions

3.1. Morphological and structural characterization

The crystallographic structure of the prepared Bi/Bi_2O_3 film was studied by X-ray diffraction (XRD) and the obtained pattern is shown in Fig. 1. Apart from the reflections coming out from the substrate (Si and Au, shown as breaks in Fig. 1) some of the diffraction peaks can be attributed to the rhombohedral metallic Bi phase (space group (S.G.) $R\bar{3}m$, JCPDS [52] 44-1246) and to the so-called α-phase of Bi_2O_3, which is monoclinic (S.G. $P2_1/c$, JCPDS 41-1449). Hence, the films consist of a mixture of metallic Bi and ceramic Bi_2O_3. According to the Rietveld refinement, the volume percentage of Bi and α-Bi_2O_3 are 70% and 30%, respectively.

On-top scanning electron microscope (SEM) images of Bi/Bi_2O_3 metal–metal oxide composite were obtained before the nanoindentation tests, as shown in Fig. 2. At low magnification, the films display uniform porosity over the entire surface (Fig. 2a). A close-up observation reveals the existence of micron-sized pores (Fig. 2b).

Remarkably, the pore walls are not dense but inherently porous. Hence, the films are hierarchically porous. An on-top SEM image after the nanoindentation tests is shown in Fig. 2c. The nanoindentation experiments left as a result an ordered array of indentations with inverted pyramid geometry. At high magnification, Fig. 2c reveals compaction of the material in the indented regions. A higher degree of compaction appears at the center of the imprint than at the edges; this is because at the center of the indentation, the applied compressive stress is larger.

3.2. Effect of compaction and strain rate

As aforementioned, different nanoindentation tests were performed at two different loading rates in order to see how the mechanical properties were modified as a function of this parameter. The penetration depth corresponding to the maximum force (approximately 12 μm) is the maximum penetration depth that can be obtained without having an influence of the substrate on the mechanical properties, according to the expression [40]:

$$h_{max} \leq \frac{d}{10} \tag{8}$$

where d is the sample's thickness (130 μm in the present study).

The influence of the loading rate on the indentation tests can be explained from Fig. 3a and b, where the variation of the applied

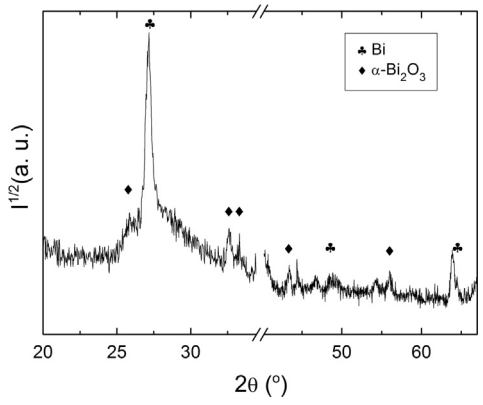

Fig. 1. XRD pattern of the Bi/Bi_2O_3 composite. Characteristic peaks of metallic bismuth and α-Bi_2O_3 are observed.

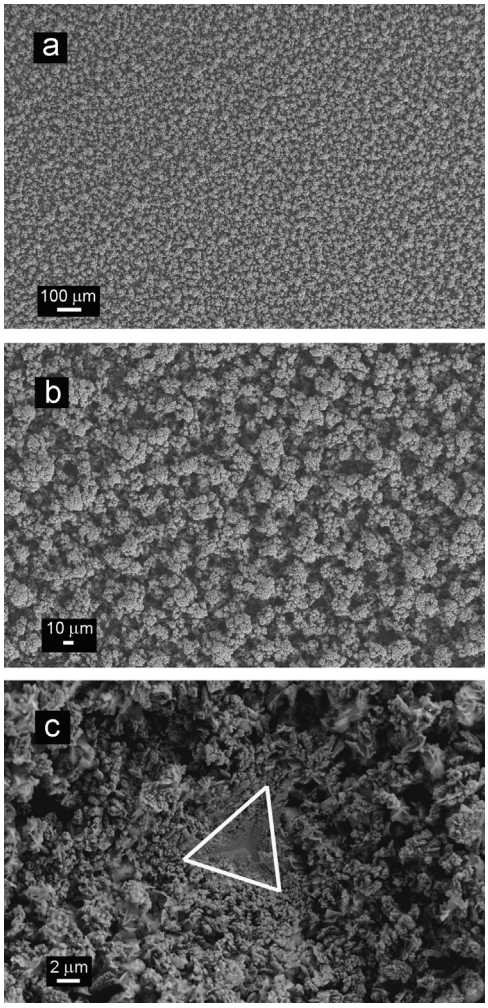

Fig. 2. SEM on-top images of the Bi/Bi_2O_3 composite (a) and (b) before nanoindentation, where porosity over the entire surface is observed and (c) after nanoindentation, where the print of the Berkovich nanoindenter due the compaction of the sample is observed.

force is plotted as a function of time. The results reveal that the unloading time is higher for the slow test and smaller for the fast test.

The strain rate ($\dot{\varepsilon}$) gives an idea of the deformation of the material in the neighborhood of a certain point and it is defined as

$$\dot{\varepsilon} = \frac{d\varepsilon}{dt} \tag{9}$$

where ε is the strain ($\varepsilon = (dh/h)$), so that [53]

$$\dot{\varepsilon} = \frac{\dot{h}}{h} = \frac{dh/dt}{h} \tag{10}$$

where h is the penetration depth. The strain rate values obtained in this work were determined using Eq. (10). The strain rate values at the end of the loading segment were corresponding to 4 mN from the load–displacement curves for the different velocities, as shown in Table 1.

From Fig. 3c and d it can be seen that the maximum penetration depth reached during the fast test is lower than the one reached in the slow tests, indicating larger hardness when the loading rate of the indentation is higher. From these curves, the unloading slope, S, has been plotted as a function of the applied force and rate, as shown in Fig. 4a. Using the method of Oliver and Pharr, both E_r and H were determined, as shown in Fig. 4b and c, respectively. As can be seen from Fig. 4b, the reduced Young's modulus depends on the applied force (and therefore on the penetration depth). Larger values of E_r are observed for higher loads, particularly at the fast rate. Interestingly, a linear relation between E_r and H is also encountered (Fig. 4c).

A correlation between the porosity volume fraction (P_{or}) and the mechanical properties (E_r and H) can be established; S, E_r and H increase as the applied force increases (i.e. when the degree of compaction is higher). It is known from finite element calculations that Poisson's ratio of porous ceramic materials does not change significantly as a function of porosity [54] and, therefore, a constant value of 0.22 (according to the volume percentage of Bi and α-Bi_2O_3 and their corresponding Poisson's ratio) was used in all calculations.

Porosity level is known to have a strong influence on the elastic constants of metallic and ceramic materials [55] and, in a first approximation, it has been shown that [56] :

$$\frac{E_{porous}}{E_{bulk}} = \left(\frac{\rho_{porous}}{\rho_{bulk}}\right)^n \tag{11}$$

where the right-hand term of Eq. (11) is the relative density and the coefficient n depends on the material (we took $n=2$ because our sample presents an open-cell porosity [34,38]). This relative density can be related to the material porosity volume fraction P_{or} [55]:

$$\frac{\rho_{porous}}{\rho_{bulk}} = 1 - P_{or} \tag{12}$$

Combining Eqs. (11) and (12) it is possible to give a first approximation of the degree of porosity of the studied sample as a function of the elastic modulus:

$$P_{or} = 1 - \left(\frac{E_{porous}}{E_{bulk}}\right)^{1/n} \tag{13}$$

Actually it is well known that even a low degree of porosity typically leads to a drastic reduction in E_r [57]. This effect is considered in the approach by Ramakrishnan and Arunachalam, which takes into account the intensification of pressure at the surface of spherical pores due to interactions between the pores and the surrounding bulk solid material [57]. For a given porosity fraction, the elastic modulus of the porous material (E_{porous}) is related to the elastic modulus of the fully dense material (E_{bulk}) according to:

$$\frac{E_{porous}}{E_{bulk}} = \frac{(1-P_{or})^2}{1+2P_{or}-3\nu P_{or}} \tag{14}$$

where ν is Poisson's ratio of the bulk non–porous material. Solving Eq. (14) it is possible to determine, in a more precise way, the degree of porosity of the sample. This is because Eq. (12) only considers the sample's porous density in relation to the bulk density while Eq. (14) also considers the pressure intensification at the surface of the spherical pores, as aforementioned. Nevertheless, we have observed that the difference between Eqs. (12) and (14) is not too significant as one could expect.

The value of E_{bulk} was determined using the rules of mixtures for the isostrain (IS) and the isostress (IT) conditions. These are the two limiting cases, so in our geometry E_{bulk} is probably in between. For the isostrain analysis

$$E_{bulk}^{IS} = 0.7E_{Bi} + 0.3E_{Bi_2O_3} = 43.40 \text{ GPa}$$

while for the isostress analysis

$$E_{bulk}^{IT} = \frac{E_{Bi}E_{Bi_2O_3}}{0.7E_{Bi} + 0.3E_{Bi_2O_3}} = 51.61 \text{ GPa}$$

where E_{Bi} and $E_{Bi_2O_3}$ are the elastic modulus of metallic bismuth and bismuth oxide, respectively, and 0.7 and 0.3 correspond to the

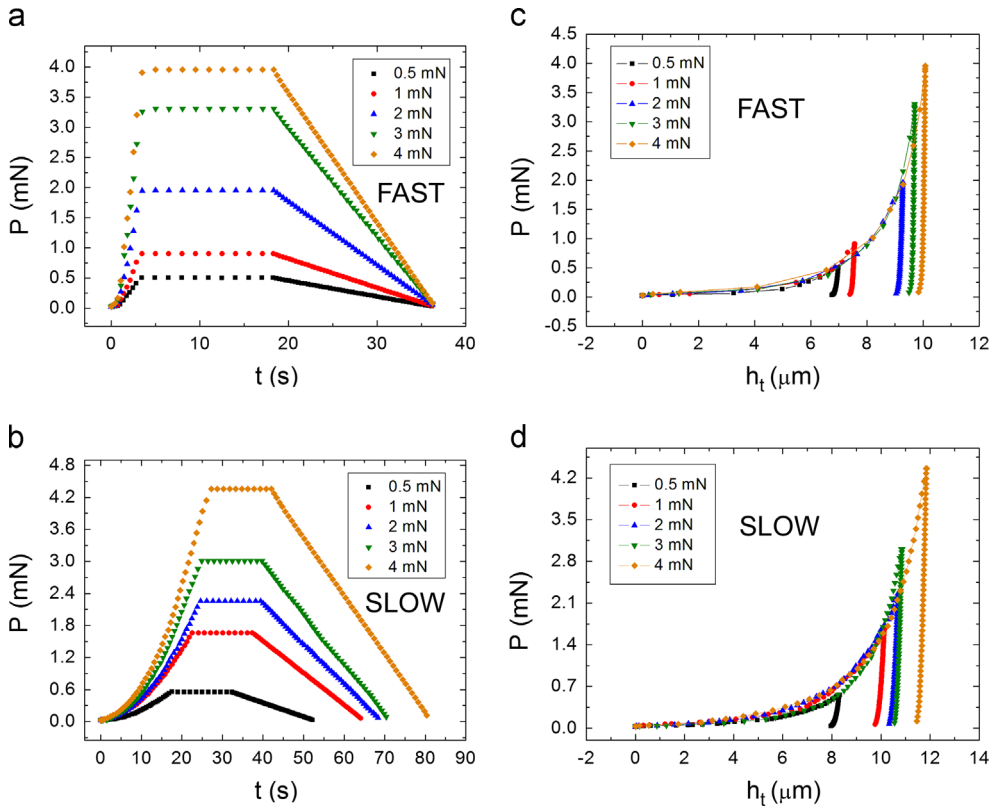

Fig. 3. Force-time curves for (a) fast and (b) slow loading rates and (c) and (d) their corresponding load–displacement curves, respectively.

Table 1
Strain rate values (s^{-1}) obtained with an applied force of 4 mN for the different loading rates.

	Strain rate (s^{-1})
Fast test	0.02833
Slow test	0.00548

volume fraction of bismuth and bismuth oxide as determined by XRD. We then assume that the elastic modulus of the metal–metal oxide composite is

$$E_{bulk} = \frac{E^{IS}_{bulk} + E^{IT}_{bulk}}{2} = 47.51 \text{ GPa}$$

These two methods used to determine the degree of porosity of the sample are based on the values of the elastic modulus obtained during the nanoindentation test.

Note that the compaction effect on porosity is more pronounced in the fast tests, as evidenced in Fig. 4b.

It can be observed that both the H and E_r values depend on the loading rate; the degree of porosity and compaction is different in each case. It can be noticed, from Table 2, that the values of the degree of porosity are very high. These values are probably overestimated because the surface of the Bi/Bi_2O_3 composite is not flat; surface roughness gives an underestimation of the values of E_{porous} and H_{porous}, which can be as much as 20% [58–60]. Hence, taking into account this effect, the values of P_{or} would be reduced down to, approximately, 70%, which are more reasonable values.

Fig. 4a shows that as the loading rate is higher, a larger value of S is obtained (which implies a smaller elastic recovery of the material). This observation can be related to the behavior of a viscoelastic non-Newtonian fluid [61].

3.3. Viscoelasticity

Creep tests for each loading rate were performed to assess the plastic deformation in porous Bi/Bi_2O_3 composite at a maximum applied force of 5 mN and with a holding segment of 600 s. The obtained data is shown in Fig. 5a and b until a maximum time of 300 and 400 s, respectively.

The variation of the penetration depth during the creep is larger for the slow loading rate ($\Delta h = 0.064$ μm) than for the fast loading rate ($\Delta h = 0.040$ μm), as evidenced from Fig. 5b, where the left y-axis refers to the penetration depth of the fast loading rate and the right y-axis refers to the penetration depth of the slow loading rate.

From Fig. 5a an anelastic behavior, analogous to the anelastic behavior of a bulk metallic glass (BMG) [62], can be observed. In BMGs this effect is explained from the occurrence of free volume. By analogy it is easy to establish a direct relation between the free volume concentration of a BMG and the pore density of a porous material. Creep behavior in BMGs was reported to depend on the loading rate [62], becoming more pronounced as the loading rate was smaller. This effect is typical of non-Newtonian fluids. Hence, the Bi/Bi_2O_3 composite exhibits a viscoelastic non-Newtonian behavior which follows the so-called three-element Voigt model. This model considers the system as a spring and a dashpot connected in parallel, which are at the same time connected in series with a second spring, as shown in Fig. 6. These elements are characterized by an elastic constant for the springs (E_1 and E_2, Fig. 6) and a viscous constant for the dashpot (η, Fig. 6).

The springs represent the elastic component ($\sigma_1 = E_1\varepsilon_1$ and $\sigma_2 = E_2\varepsilon_2$) of the material while the dashpot represents the

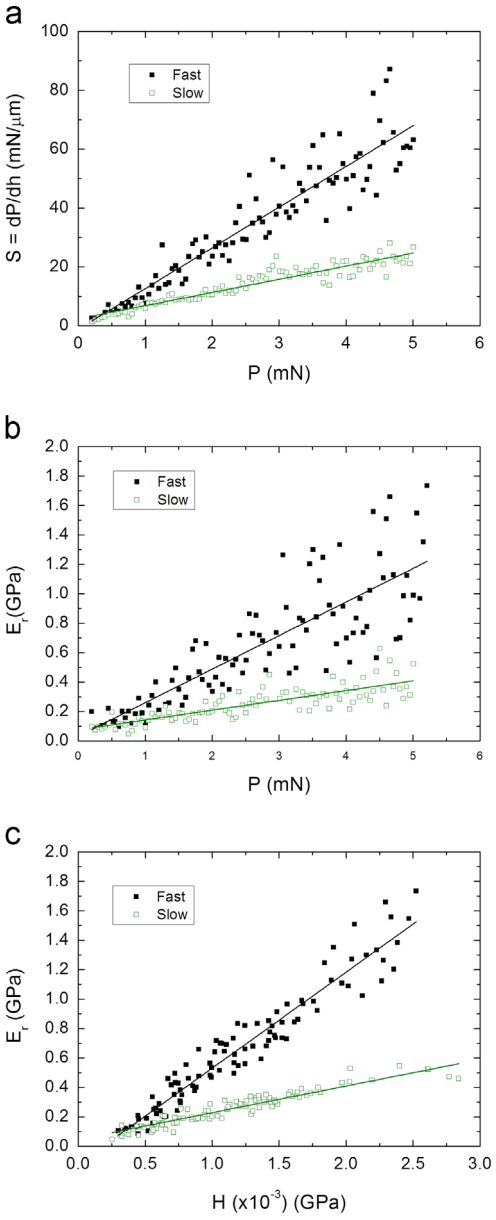

Fig. 4. Mechanical properties of the Bi/Bi_2O_3 composite (a) S vs. P (b) E_r vs. P (c) E_r vs. H. The influence of the loading rate over the mechanical properties is evidenced, obtaining larger values of both E_r and H as the loading rate increases.

Table 2
Values of the degree of porosity of the nanoindented sample as a function of the loading rate.

P (mN)	Slow		Fast	
	Eq. (11)	Eq. (12)	Eq. (11)	Eq. (12)
0.5	0.96	0.94	0.95	0.92
1	0.95	0.92	0.94	0.89
2	0.93	0.89	0.92	0.86
3	0.92	0.88	0.89	0.83
4	0.91	0.87	0.88	0.82

viscous ($\sigma_3 = \eta\dot{\varepsilon}_3$) component. This model is a modification of the so-called Kelvin and Voigt model [40], which is based on a spring and a dashpot connected in parallel. In the Kelvin–Voigt model (i.e. without E_2 in Fig. 6), the total strain, ε, is equal to the strain in

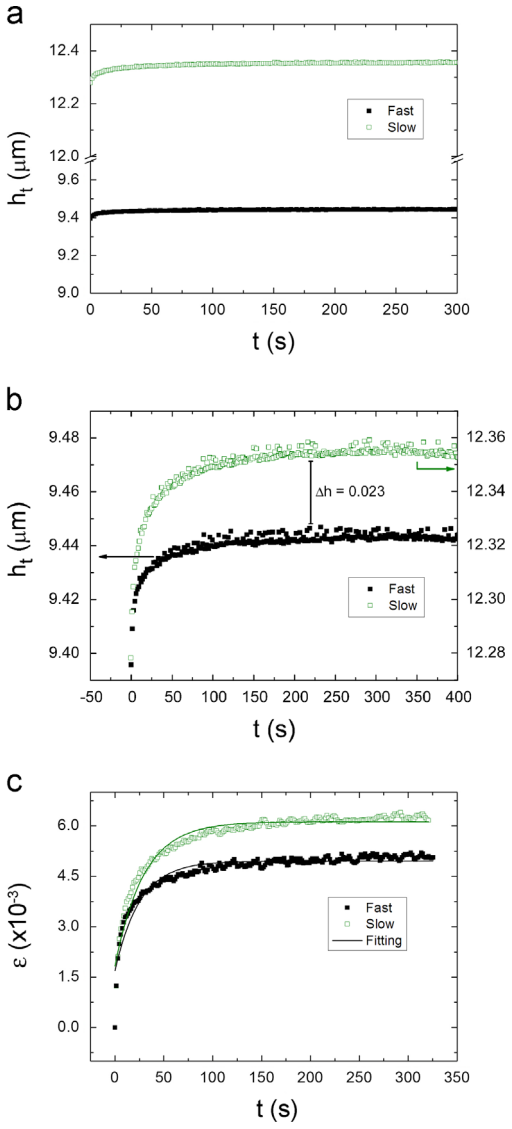

Fig. 5. (a) Time–dependence of the indenter displacement into the sample during the constant-load segment for different loading rates; (b) h vs. t normalized to the same initial starting depth during creep. The left-side scale shows the penetration depth reached by the nanoindenter for the fast loading rate while the right-side scale corresponds to the slow loading rate; (c) shows the dependence of the strain vs. t.

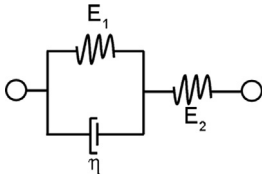

Fig. 6. Schematic representation of the three-element Voigt model, consisting in a spring connected in parallel to another spring and a dashpot, which are connected in series.

each of the components:

$$\varepsilon = \varepsilon_D = \varepsilon_S \tag{15}$$

And the applied load (σ) is supported jointly by both the spring and the dashpot:

$$\sigma = \sigma_1 + \sigma_3 \tag{16}$$

Combining Eqs. (15) and (16) with the elastic and viscous behaviors it is easy to see that

$$\sigma = \sigma_1 + \sigma_3 = E_1\varepsilon_1 + \eta\dot{\varepsilon}_3 \tag{17}$$

If the applied stress is constant (σ_0), that is, during a creep experiment:

$$\sigma_0 = E_1\varepsilon + \eta\dot{\varepsilon} = E_1\varepsilon + \eta\left.\frac{d\varepsilon}{dt}\right|_3 \tag{18}$$

the solution to Eq. (18) is

$$\varepsilon(t) = \frac{\sigma_0}{E_1}\left(1 - e^{-\lambda t}\right) \tag{19}$$

where t is time and λ is the so-called time of relaxation, defined as

$$\lambda = E_1/\eta \tag{20}$$

where η is the viscosity. If now a second spring ($E=E_2$) is connected in series to the dashpot and spring 1 (as shown in Fig. 6), Eq. (19) becomes

$$\varepsilon(t) = \frac{\sigma_0}{E_2} + \frac{\sigma_0}{E_1}\left(1 - e^{-E_1 t/\eta}\right) \tag{21}$$

Interestingly, the obtained strain vs. time curves from nanoindentation at different loading rates are well-fitted with Eq. (21), as can be seen from Fig. 5c, which confirms that the Bi/Bi_2O_3 composite shows a well-defined viscoelastic behavior. Since during nanoindentation with a Berkovich tip shear motion governs deformation, it is usual to express the mechanical constants of the model described above in terms of the shear modulus (G) [40] instead of Young's modulus. Then, from the shear modulus it is possible to determine the elastic modulus:

$$G_{eff} = \frac{E}{2(1+\nu)} \tag{22}$$

where ν is Poisson's ratio and G_{eff} the effective shear modulus, which is determined from the following expression:

$$\frac{1}{G_{eff}} = \frac{1}{G_1} + \frac{1}{G_2} \tag{23}$$

since the springs of the model (Fig. 6) are connected in parallel.

From the parameters obtained from the fitting, it has been possible to determine both E and η values, as shown in Table 3. Where the parameter a has been defined as σ_0/G_1, b has been defined as σ_0/G_2 and λ as G_1/η, being σ_0:

$$\sigma_0 = \frac{F}{f_B h^2} \tag{24}$$

where F is the applied force (5 mN), h is the penetration depth reached at that force and f_B is a function that depends on the indenter shape. For a Berkovich indenter, $f_B = 24.56$ [40].

As can be observed from Table 3, the values of the effective elastic modulus determined using the three-element Voigt model agree rather well to the values obtained experimentally. Also, from the values obtained with the three-element Voigt model, it is possible to determine the viscosity of the Bi/Bi_2O_3 sample (Eq. (20)). As can be seen from Table 3, a higher value of viscosity is obtained when the loading rate is higher. This tendency is in complete agreement with the results shown in Fig. 3c and d, where it can be observed that the penetration depth increases as the loading rate is smaller. This is because the Bi/Bi_2O_3 composite offers a major resistance to deformation when the loading rate is higher, which implies that the viscosity should be larger.

3.4. Simulation studies

Table 4 shows the mechanical properties used during simulations for the fast and slow loading rates. E in Eq. (5) was determined from the fit of the E–P evolutions shown in Figs. 4b for 0.5, 1, 2, 3 and 4 mN. Once E is determined, the corresponding hardness is found from the fitted results of E–H curves shown in Fig. 4c. Finally, it is assumed that $\sigma_{ys}=H$ and $\sigma_{ys}=H/3$. To trigger each different set of mechanical properties, we created different stages of penetration depth. The maximum penetration depth of each stage corresponded to the load at which E and σ_{ys} change. This maximum penetration depth was determined through the experimental P–h_s curves shown in Fig. 7.

From Fig. 7 it can be seen that $\sigma_{ys}=H/3$ is a better assumption than $\sigma_{ys}=H$. Moreover, Fig. 7 reveals that the simulations with the elastic–perfectly plastic model share the same features as the experiments. In Fig. 7b simulations overestimate the experiment, although the (h_{max},P_{max}) points from simulations and experiments agree quite well. On the contrary, from Fig. 7a it is obvious that the simulation (with $\sigma_{ys}=H/3$) is underestimating the experimental curve and the (h_{max},P_{max}) point is not captured anymore. However, by incorporating the Drucker–Prager (DP) model into the simulation for the fast loading rate the agreement between simulation and experiment improves and the trend becomes analogous to what is seen in Fig. 7b. This suggests that depending on the loading rate, the material response is different. For small loading rate it appears that the material deforms according to an elastic–perfectly plastic model. Once the loading rate reaches a certain value, a frictional component with a DP model is needed to properly account for the deformation mechanism.

These FE simulation results are in agreement with the viscoelastic behavior of the sample. They show, as aforementioned, that is necessary to introduce a friction parameter (DP) when the loading rate increases, which indicates that the viscosity of the metal–ceramic composite changes with the loading rate.

Table 4
Values of the elastic modulus and the yield stress for different values of applied load at different loading rates, with a friction angle of 20°.

P (mN)	Slow		Fast		β
	E (MPa)	σ_{ys} (MPa)	E (MPa)	σ_{ys} (MPa)	
0	128	0.15	53	0.08	20°
1	186	0.26	278	0.20	
2	244	0.37	503	0.32	
3	302	0.47	728	0.44	
4	360	0.58	953	0.56	

Table 3
Values of the Voigt model fitting parameters, shear modulus, viscosity and elastic modulus at an applied force of 5 mN for the different indentation loading rates.

	Adjusting parameters			Shear modulus (GPa)			E_{eff} (GPa)		η (GPa s)
	a	b	λ (s^{-1})	G_1	G_2	G_{eff}	Theoretical	Experimental	
Fast	0.00169	0.00326	0.0393	1.3508	0.7002	0.4612	1.1253	0.9898	34.37
Slow	0.00183	0.00429	0.03396	0.7289	0.3109	0.2179	0.5318	0.5029	21.46

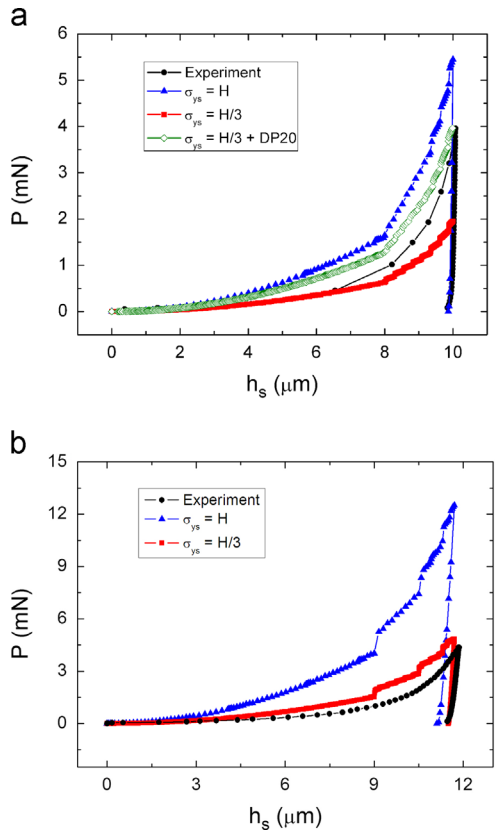

Fig. 7. FE simulations of the loading-displacement curves for (a) fast (where a Drucker–Prager coefficient, DP, has been introduced in order to consider a frictional parameter) and (b) slow loading rates.

4. Conclusions

Porous Bi/Bi_2O_3 composite films have been grown by one-step electrodeposition in acidic electrolyte to favor hydrogen evolution and, hence, the creation of porosity. The films are rather rough and exhibit porosity along the entire surface, as confirmed by SEM. Concerning the structural characterization, XRD analyses reveal that the composite film shows characteristic peaks of metallic Bi, which is rhomohedral, and the so-called α-phase of Bi_2O_3 (or bismite), which is monoclinic.

The nanomechanical properties of the Bi/Bi_2O_3 composite film have been studied as a function of the loading rate and maximum applied load. The nanoindentation assays reveal that, for a given applied force, the penetration depth is larger as the loading rate is made lower. In turn, the elastic modulus increases with the loading rate. From the E_r and H values obtained from nanoindentation tests, the degree of porosity has been determined. The obtained values of porosity are probably overestimated since the models existing in the literature do not take into account the existence of surface roughness.

Strain rate has also been determined and has been observed to increase with the increase of loading rate. Creep tests have also been performed, revealing an anelastic behavior of the sample that follows a non-Newtonian viscoelastic behavior, which can be well-fitted by the strain equation of the three-element Voigt model. Finally, the experimental results have been compared with those obtained by FE simulations, and a relatively good agreement between the measured and the calculated nanoindentation curves has been obtained. For the fast loading rate, the Drucker–Prager (DP) model has been incorporated to account for the increase of viscosity (considering the analogy between our nanoporous composite and a non-Newtonian viscoelastic material).

The present paper provides insight into the deformation mechanisms of a novel class of material, consisting of a highly-porous metal–ceramic composite, that can be used in diverse applications, ranging from purely structural/mechanical (e.g. as impact damper) or in hybrid platforms for photocatalysis and other physico-chemical applications.

Acknowledgments

The authors wish to acknowledge the financial support from the MAT2011-27380-C02-01 research project from the Spanish MINECO and the 2014-SGR-1015 project from the Generalitat de Catalunya. M.D.B. was partially supported by an ICREA-Academia award. E.P. acknowledges the Spanish MINECO for the 'Ramon y Cajal' contract (RYC-2012-10839). M. G. acknowledges the support of the Secretary for Universities and Research of the Government of Catalonia and the COFUND programme of the Marie Curie Actions of the 7th R&D Framework Programme of the European Union for the 'Beatriu de Pinos' contract (2013 BP-B 00077).

References

[1] J. Liu, L. Cao, W. Huang, Z. Li, ACS Appl. Mater. Interfaces 3 (2011) 3552–3558.
[2] K. Otsubo, T. Haraguchi, O. Sakata, A. Fujiwara, H. Kitagawa, J. Am. Chem. Soc. 134 (23) (2012) 9605–9608.
[3] Q. Xiong, J. Tu, Y. Lu, J. Chen, Y. Yu, X. Wang, C. Gu, J. Mater. Chem. 22 (35) (2012) 18639–18645.
[4] T.N. Huan, T. Ganesh, K.S. Kim, S. Kim, S.-H. Han, H. Chung, Biosens. Bioelectron. 27 (1) (2011) 183–186.
[5] W. Sun, N.P. Kherani, K.D. Hirschman, L.L. Gadeken, P.M. Fauchet, Adv. Mater. 17 (10) (2005) 1230–1233.
[6] J.L.C. Rowsell, O.M. Yaghi, Microporous Mesoporous Mater. 73 (1–2) (2004) 3–14.
[7] F. Scaglione, P. Rizzi, L. Battezzati, J. Alloy. Compd. 536 (2012) S60–S64.
[8] V. Bansal, H. Jani, J. Du Plessis, P.J. Coloe, S.K. Bhargava, Adv. Mater. 20 (4) (2008) 717–723.
[9] X. Xia, J. Tu, X. Wang, C. Gu, X. Zhao, J. Mater. Chem. 21 (3) (2011) 671–679.
[10] K. Rezwan, Q.Z. Chen, J.J. Blaker, A.R. Boccaccini, Biomaterials 27 (18) (2006) 3413–3431.
[11] J. Banhart, Prog. Mater. Sci. 46 (6) (2001) 559–632.
[12] L.P. Lefebvre, J. Banhart, D.C. Dunand, Adv. Eng. Mater. 10 (9) (2008) 775–787.
[13] Y. Ren, Z. Ma, P.G. Bruce, Chem. Soc. Rev. 41 (14) (2012) 4909–4927.
[14] P. Yang, D.I. Margolese, Nature 396, (1998) 6–9.
[15] S. Ko, D. Lee, S. Jee, H. Park, K. Lee, W. Hwang, Thin Solid Films 515 (4) (2006) 1932–1937.
[16] L. Vojkuvka, a. Santos, J. Pallarès, J. Ferré-Borrull, L.F. Marsal, J.P. Celis, Surf. Coatings Technol 206 (8–9) (2012) 2115–2124.
[17] C. Cheng, a.H. W. Ngan, Appl. Phys. Lett. 102 (21) (2013) 213119.
[18] X. Lang, T. Qiu, K. Long, D. Han, H. Nan, P.K. Chu, Nanotechnology 24 (25) (2013) 255303.
[19] G.A. Crawford, N. Chawla, K. Das, S. Bose, A. Bandyopadhyay, Acta Biomater. 3 (3) (2007) 359–367.
[20] F. Schmidt-Stein, S. Thiemann, S. Berger, R. Hahn, P. Schmuki, Acta Mater. 58 (19) (2010) 6317–6323.
[21] H. Hirakata, K. Ito, A. Yonezu, H. Tsuchiya, S. Fujimoto, K. Minoshima, Acta Mater. 58 (15) (2010) 4956–4967.
[22] J.N. Kondo, K. Domen, Chem. Mater. 20 (2008) 835–847.
[23] F. Jiao, J. Jumas, M. Womes, A.V. Chadwick, A. Harrison, P.G. Bruce, S. Andrews, F. Ky, L. Agre, J. Am. Chem. Soc. 128 (39) (2006) 12905–12909.
[24] M. Grätzel, Nature 414, (2001) 338–344.
[25] A. Goetzberger, C. Hebling, H.-W. Schock, Mater. Sci. Eng. R Rep. 40 (1) (2003) 1–46.
[26] A.J. Frank, N. Kopidakis, J. Van De Lagemaat, Coord. Chem. Rev. 248 (13–14) (2004) 1165–1179.
[27] M. Vettraino, M. Trudeau, D.M. Antonelli, Inorg. Chem. 40 (16) (2001) 2088–2095.
[28] C. Yue, M. Trudeau, D. Antonelli, Chem. Commun. 18 (2006) 1918–1920.
[29] C. Yue, L. Qiu, M. Trudeau, D. Antonelli, Inorg. Chem. 46 (12) (2007) 5084–5092.
[30] P. Qiao, M. Yang, F. Bobaru, J. Aerosp. Eng. 21 (4) (2008) 235–248.
[31] E. Linul, L. Marsavina, T. Voiconi, T. Sadowski, J. Phys. Conf. Ser. 451 (2013) 012002.
[32] N.G. Chechenin, J. Battiger, Thin Solid Films 261 (1995) 219–227.
[33] M. Guerrero, S. Pané, B.J. Nelson, M.D. Baró, M. Roldán, J. Sort, E. Pellicer, Nanoscale 5 (24) (2013) 12542–12550.
[34] D. Bellet, A. Lamagnère, A. Vincent, Y. Bréchet, J. Appl. Phys. 80 (7) (1996) 3772.
[35] Z. Fang, M. Hu, W. Zhang, X. Zhang, H. Yang, Thin Solid Films 517 (9) (2009) 2930–2935.

[36] J. Yan, H. Takahashi, X. Gai, H. Harada, J. Tamaki, T. Kuriyagawa, Mater. Sci. Eng. A 423 (1–2) (2006) 19–23.
[37] A. Varea, E. Pellicer, S. Pané, B.J. Nelson, S. Suriñach, M.D. Baró, J. Sort, Int. J. Electrochem. Sci. 7 (2012) 1288–1302.
[38] J. Biener, A.M. Hodge, A.V. Hamza, L.M. Hsiung, J.H. Satcher, J. Appl. Phys. 97 (2) (2005) 024301.
[39] T. Watanabe, K. Muratsubaki, Y. Benino, H. Saitoh, T. Komatsu, J. Mater. Sci. 36 (2001) 2427–2433.
[40] A.C. Fischer-Cripps, Nanoindentation, Springer, New York, 2004.
[41] N.A. Fleck, H. Otoyo, A. Needleman, Int. J. Solids Struct. 29 (1992) 1613–1636.
[42] X. Chen, Y. Xiang, J.J. Vlassak, J. Mater. Res. 21 (03) (2011) 715–724.
[43] X. Lu, P. Xiao, H. Li, Acta Metall. Sin. 25 (5) (2012) 383–390.
[44] Y.-J. Kim, D.-H. Bae, Y.-J. Kim, Key Eng. Mater. 297–300 (2005) 1050–1055.
[45] W.C. Oliver, G.M. Pharr, J. Mater. Res. 7 (1992) 1564–1583.
[46] The Rietveld Method, in: R.A. Young (Ed.), OUP/International Union Crystallography, Oxford, 1995.
[47] A.C. Fischer-Cripps, Surf. Coatings Technol. 200 (14–15) (2006) 4153–4165.
[48] ABAQUS 2014. Dassault Systèmes.
[49] M. Karakus, R.J. Fowell, Tunneling Undergr. Sp. Technol. 18 (2003) 513–523.
[50] T.F. Guo, J. Faleskog, C.F. Shih, J. Mech. Phys. Solids 56 (2008) 2188–2212.
[51] P. Clément, S. Meille, J. Chevalier, C. Olagnon, Acta Mater. 61 (2013) 6649–6660.
[52] PCPDF WIN Software. 2013.
[53] V. Maier, K. Durst, J. Mueller, B. Backes, H.W. Höppel, M. Göken, J. Mater. Res. 26 (11) (2011) 1421–1430.
[54] A.P. Roberts, E.J. Garboczi, J. Am. Ceram. Soc. 83 (2000) 3041–3048.
[55] E. Tolu, S. Garroni, E. Pellicer, J. Sort, C. Milanese, P. Cosseddu, S. Enzo, M.D. Baró, G. Mulas, J. Mater. Chem. C 1 (32) (2013) 4948–4955.
[56] E. Pellicer, S. Pané, V. Panagiotopoulou, S. Fusco, K.M. Sivaraman, S. Suriñach, M.D. Baró, B.J. Nelson, J. Sort, Int. J. Electrochem. Sci. 7 (5) (2012) 4014–4029.
[57] N. Ramakrishnan, V.S. Arunachalam, J. Am. Ceram. Soc. 76 (1993) 2745–2752.
[58] E. Donnelly, S.P. Baker, A.L. Boskey, M.C.H. van der Meulen, J. Biomed. Mater. Res. A 77 (2) (2006) 426–435.
[59] W.-G. Jiang, J.-J. Su, X.-Q. Feng, Eng. Fract. Mech. 75 (17) (2008) 4965–4972.
[60] J.-Y. Kim, S.-K. Kang, J.-J. Lee, J. Jang, Y.-H. Lee, D. Kwon, Acta Mater. 55 (10) (2007) 3555–3562.
[61] R.P. Chhabra, in: A.P. Deshpande, J. Murali Krishnan, P.B. Sunil Kumar (Eds.), Non-Newtonian Fluids: An Introduction, Rheology of Complex Fluids, Springer, Munich, 2010, pp. 1–33 (Chapter 1).
[62] A. Concustell, J. Sort, A.L. Greer, M.D. Baró, Appl. Phys. Lett. 88 (2006) 171911.